Journal of Materials Chemistry A

ROYAL SOCIETY OF CHEMISTRY

PAPER

View Article Online
View Journal | View Issue

Cite this: J. Mater. Chem. A, 2025, 13, 22755

Enhancing zinc-ion energy storage: impact of MOF-5 derived carbonization temperature on performance†

Wojciech Kukułka, [ab] Verónica Montes-García, [ab] Saira Sarwar, [b] Dawid Pakulski, [b] Paolo Samorì *[a] and Artur Ciesielski *[ab]

Received 27th April 2025
Accepted 29th May 2025

DOI: 10.1039/d5ta03330f

rsc.li/materials-a

We report the carbonization of metal–organic framework-5 (MOF-5) at various temperatures to investigate the correlation between physicochemical properties and electrochemical performance in zinc-ion energy storage. The sample carbonized at 1000 °C exhibits the highest specific capacitance (268.93 F g^{-1}), energy density (166.9 W h kg^{-1}), and power density (9234 W kg^{-1}), attributed to increased porosity, enhanced graphitization, and reduced charge transfer resistance. This simultaneous achievement of high energy and power densities underscores the potential of carbonized MOF-5 (CMOF-5) as a high-performance nanostructured electrode material for advanced energy storage devices.

The intermittent nature of renewable energy sources, which has become evident in the context of the nowadays energy crisis, demands the development of more and more efficient energy storage systems (ESSs) to guarantee a consistent and sustainable energy supply.[1–3] Among the various technologies being explored, zinc ion-based energy storage systems (Zn-ESS) have emerged as a promising alternative due to their high theoretical capacity, abundance, low cost, and environmental friendliness.[4–6] Zinc metal, in particular, is an attractive anode material due to its high volumetric capacity, non-toxicity, and relatively low redox potential, making it a viable candidate for large-scale energy storage applications. However, to achieve an optimal energy storage system, the selection of a suitable cathode material remains a crucial challenge.[7–9]

Several cathode materials have been investigated for Zn-ESS, including manganese dioxide (MnO_2),[10] vanadium-based compounds,[11] and Prussian blue analogs (PBAs).[12] While these materials exhibit reasonable electrochemical performance, they suffer from intrinsic limitations such as dissolution in electrolytes, structural instability, and sluggish reaction kinetics, which compromise the long-term cycling stability of the system. In contrast, activated carbon (AC)[13] has gained significant attention as a cathode material due to its excellent electrical conductivity, high surface area, and stability in aqueous electrolytes. However, as a pure electrical double-layer capacitor (EDLC) material, activated carbon exhibits a relatively low energy density, which limits its overall potential in high-performance Zn-ESS.

Metal–organic frameworks (MOFs), a continuously expanding family of crystalline porous nanostructured materials, are establishing themselves as ideal cathode materials owing to their unique characteristics.[14] These features include nanoscale controlled composition and structure, substantial surface area, and exceptional porosity. Additionally, controlled carbonization or pyrolysis of MOFs can enhance their electrical conductivity by forming a porous carbon-based framework that can host metal species while retaining their inherent porosity.

Within the large portfolio of available MOFs, those Zn-based offer several advantages, including the acceleration of Zn^{2+} ion kinetics and enhanced charge transfer capabilities. MOF-5, comprising Zn^{2+} ions connected by terephthalic acid, stands out as one of the archetypical MOFs, playing a significant role in the development of the broader field of metal–organic frameworks. The carbonization process of MOF-5 initially yields ZnO components, which are progressively eliminated through diffusion from the MOF-5 framework as the duration and temperature of carbonization are increased. Importantly, recent reports indicate that above a specific carbonization temperature, a process known as carboreduction takes place, wherein ZnO species undergo a gradual transformation into metallic Zn.[15–17] The removal of ZnO and Zn species during carbonization could potentially create pore channels with sizes suitable for accommodating Zn^{2+} ions from the electrolyte during the discharging process, thereby enhancing ion accessibility and transport within the electrode. The presence of these species may also contribute to the energy storage mechanism, potentially increasing the energy density of the cathode material. Thus, the interplay between Zn and ZnO retention, pore

[a]Université de Strasbourg, CNRS, ISIS UMR 7006, 8 allée Gaspard Monge, Strasbourg 67000, France. E-mail: samori@unistra.fr; ciesielski@unistra.fr

[b]Center for Advanced Technologies, Adam Mickiewicz University, Uniwersytetu Poznaskiego 10, Poznań, 61-614, Poland

† Electronic supplementary information (ESI) available. See DOI: https://doi.org/10.1039/d5ta03330f

formation and electrochemical performance remains a key aspect to be explored, and optimization of the carbonization temperature can determine the relationship between structural properties and electrochemical activity.

Here, we report on the synthesis and characterization of carbonized MOF-5 as a nanostructured cathode material for Zn-ESS. The effect of carbonization at various temperatures ranging from 600 to 1000 °C is explored, and the resulting MOF-derived carbons' physicochemical properties including surface area, pore size, electrical conductivity, and Zn/ZnO ratio are correlated with the observed electrochemical performance. Distinct from previous MOF carbonization studies, our work provides a comprehensive and temperature-resolved analysis of zinc species evolution, including ZnO formation, carboreduction to metallic Zn, and eventual evaporation, supported by X-ray photoelectron spectroscopy (XPS), X-ray diffraction (XRD), scanning electron microscopy (SEM), thermogravimetric analysis (TGA), and Raman spectroscopy. While prior studies such as the studies by Shin *et al.*[18] and Wang *et al.*[19] have demonstrated temperature-dependent porosity control in Zn-MOF-5-derived carbons for lithium–air batteries and electrochemical capacitors, these studies primarily emphasized porosity tuning or etching strategies without a detailed investigation of metal phase evolution. In contrast, this study systematically investigates the evolution of Zn and ZnO species during carbonization over the temperature range of 600–1000 °C, establishing clear correlations between their phase transformations and key material properties, including graphitization, pore architecture, and electrochemical behaviour in Zn-ESS. This integrated structure–function perspective highlights how controlling the residual Zn content can be leveraged to tune conductivity and ion accessibility, offering new insights into the design of MOF-derived carbon electrodes for high-performance Zn-based energy storage.

The pristine MOF-5 material is synthesized through a solvothermal method by using a modified reported procedure by Park *et al.* (see ESI for details, and Fig. S1†).[20] MOF-5 is then carbonized (CMOF-5) under an inert atmosphere at different temperatures, ranging from 600 to 1000 °C (Fig. 1). To explore the carbonization mechanism of MOF-5, SEM is first employed to examine the nanoscale morphology, specifically the size, shape, and surface structure, of CMOF-5 samples. Fig. 2 and S2† reveal that the CMOFs assemble into large cubic aggregates with lateral sizes ranging between 10 and 25 μm. Such unique morphology is retained regardless of the carbonization temperature, yet the temperature plays a pivotal role in the surface structure of the resulting materials.[17] CMOF-5 materials obtained at 600 °C and 700 °C exhibit noticeable ZnO agglomerates on their surfaces. Upon reaching 800 °C, the agglomerates become larger, displaying cracks and defects in the cubic CMOF-5 structures, as well as small Zn or ZnO islands on their surface. This indicates that a significant portion of the ZnO has been removed from the CMOF-5 core structure, forming large agglomerates on the surface. Additional pores and defects in the carbon structure are simultaneously created during the ZnO migration to the CMOF-5 surface (see later Raman and BET characterizations). At 900 °C, the large agglomerates disappear, leaving only small Zn or ZnO clusters. Upon further heating to 1000 °C, all zinc species are evaporated and removed from the CMOF-5 structure. Fig. S3† shows the XRD diffractograms of all the carbonized samples. In agreement with SEM results, the samples produced at carbonization temperatures ranging from 600 to 900 °C display the characteristic sharp peaks attributed to ZnO.[21–23] Importantly, when the carbonization temperature reaches 1000 °C no traces of ZnO are observed, confirming the complete Zn removal of the MOF-derived carbon structure. In order to quantify the amount of Zn and ZnO on the CMOF-5 samples and the defectiveness of each sample, XPS investigations, TGA and Raman spectroscopy are then performed (Fig. S4–S7†). XPS provides insights into the surface composition with a penetration depth of 1–10 nm, whereas TGA offers information on the composition throughout the entire sample. Fig. S4† shows the XPS survey spectra of all CMOF-5 samples, normalized by the carbon peak. With the rising carbonization temperature, a gradual increase in the presence of Zn and ZnO on the surface of CMOF-5 is observed, reaching its peak value for the sample carbonized at 800 °C, in line with SEM and XRD characterization. Subsequently, there is a reduction in the amount of Zn and ZnO present on the sample obtained at 900 °C and at 1000 °C, with a complete evaporation of the Zn species occurring due to the carboreduction process. Table S1† reports the quantitative data indicating the atomic proportions of each element present on the surface of all the carbonized samples, especially Zn/O ratio. While this ratio amounts to 0.57 for samples treated at carbonization temperatures of 600 and 700 °C, it rises up to 0.83 at 800 °C, due to the

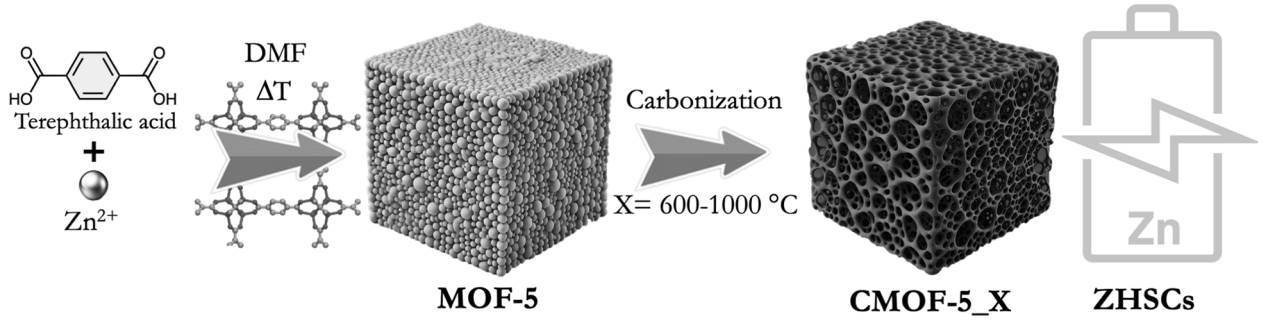

Fig. 1 Synthetic pathway of CMOF-5_*X* samples, with *X* being the carbonization temperature.

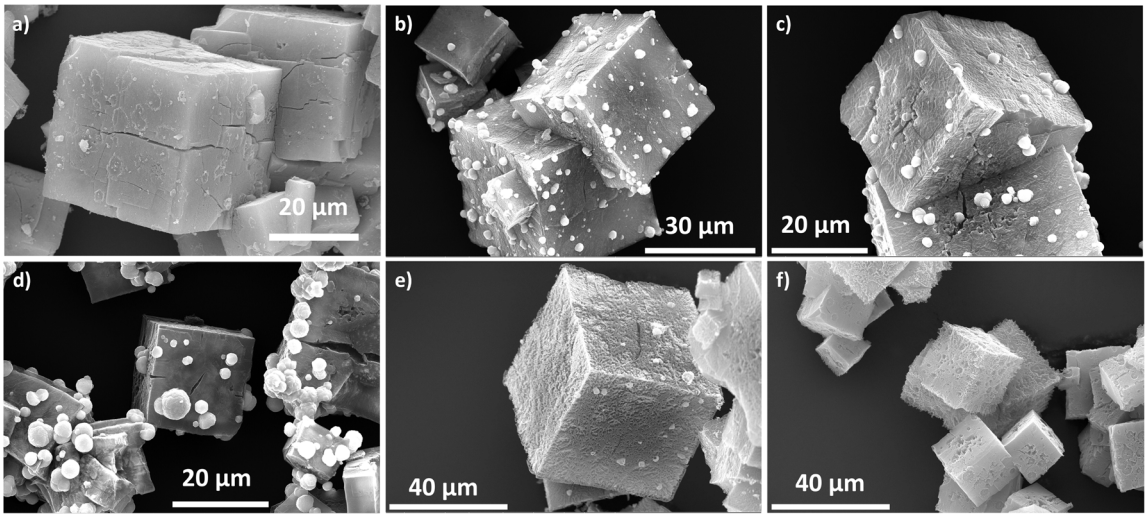

Fig. 2 SEM images of (a) MOF-5 and CMOF-5 carbonized at: (b) 600 °C, (c) 700 °C, (d) 800 °C, (e) 900 °C and (f) 1000 °C.

formation of metallic Zn. Subsequently, at 900 °C, the evaporation of metallic Zn begins (as the approximated evaporation temperature of Zn is 907 °C), leading to a reduction in the Zn/O ratio to 0.72. Finally, at a carbonization temperature of 1000 °C, all Zn species, including the ZnO integrated into the porous carbon matrix, disappear. TGA is then performed to assess the overall composition of the CMOF-5 samples, as depicted in Fig. S5.† As observed in the TGA analysis of MOF-5 (Fig. S1d†) and in agreement with previous reports, within the temperature range of 400–550 °C, the organic ligand undergoes thermal decomposition, generating gases such as carbon monoxide, carbon dioxide, and benzene. This process leads to the creation of a carbon matrix, maintaining the original MOF-5 structure (Fig. 2 and S2†). Simultaneously, Zn_4O clusters start transforming into ZnO at this stage.[17] As can be seen in Fig. S5,† the samples carbonized within the range of 600–800 °C display a comparable composition, comprising approximately 77% Zn and ZnO in weight. In contrast, the sample carbonized at 900 °C exhibits a notably reduced presence of zinc species, accounting for approximately 53% in weight, in full agreement with SEM, XRD and XPS. This is a clear indication of the occurrence of carboreduction. Briefly, the carbon species actively remove oxygen from the ZnO, resulting in the reduction of ZnO to metallic Zn and the production of carbon oxides (such as CO and CO_2) as byproducts. Upon increasing the carbonization temperature to 1000 °C, the zinc species are entirely evaporated (boiling point of Zn metal is 907 °C) from the material's structure, rendering the sample completely composed of porous carbon. The Raman spectra of CMOF-5 samples (Fig. S6 and S7†) are deconvoluted by using five Lorentzian curves, which consist of the first-order Raman modes, namely: D, G, D′, D″ and D* (Fig. S6†), in an analogous manner to other carbon-based materials. The D band typically arises from the breathing modes of sp^3-hybridized carbon atoms, and it is associated with the presence of defects and disorder in the carbon lattice. Conversely, the G band corresponds to the E_{2g} mode of sp^2-hybridized carbon atoms and is indicative of the graphitic structure and the degree of order in the carbon lattice. The intensity ratio of D and G bands (I_D/I_G) (Fig. S7a†) is frequently utilized to quantify the extent of disorder in carbon-based materials. At 600 °C and 700 °C carbonization temperatures, the I_D/I_G ratio remains below 1.35, indicating a structure primarily composed of graphite-like carbon with a well-ordered arrangement.[24] However, this trend shifts at 800 °C, where the I_D/I_G ratio reaches 1.65, indicating an increase in structural defects, in agreement with SEM analysis. This increase can be attributed to the extraction of zinc species from the core structure of the CMOF-5, which, while migrating to the surface, induces the formation of defects and new nanoscale pores along their path. Interestingly, at 900 °C and 1000 °C, the I_D/I_G ratio decreases, possibly due to carbon self-healing processes occurring at higher temperatures, consequently reducing the number of structural defects.[25] The additional bands (D′, D″ and D*) originate from the defects within the graphitic framework of the carbon material. The $I_{D'}/I_G$, $I_{D''}/I_G$, and I_{D*}/I_G ratios are shown in Fig. S7b, c and d† respectively. The $I_{D'}/I_G$ and $I_{D''}/I_G$ ratios follow the same trend as the I_D/I_G ratio with a maximum disorder reached when 800 °C is used as carbonization temperature. The specific surface area and total pore volume of all samples are assessed by using nitrogen adsorption/desorption isotherms shown in Fig. S8.† The isotherms of the CMOF-5 samples exhibit a type IV shape, indicating the presence of both micro- and mesopores within the materials. This coexistence of different pore sizes renders these materials well-suited for energy storage applications.[26–28] Additionally, all isotherms display an H3 type hysteresis loop, which is indicative of loosely assembled particles that form slit-like pores.[29] The specific surface area and total pore volume values for all samples are reported in Table S2.† The samples carbonized within the range of 600–800 °C demonstrate constrained surface areas and pores due to the presence of zinc species, as indicated by their similar BET-specific surface area and total pore volume values. However, when the carbonization of MOF-5 is performed at 900 °C, both the values of specific surface area

and pore volume are significantly increased and can be attributed to the extraction of zinc species from the CMOF-5 core, thereby releasing the occupied space. Notably, the material carbonized at 1000 °C consists only of highly porous carbon frameworks, with a specific surface area of 2151 $m^2 g^{-1}$ and fully accessible pores (1.87 $cm^3 g^{-1}$). Consequently, the BET findings align entirely with the findings from the SEM, XRD, XPS and Raman analyses, by confirming the removal of zinc species during carbonization at temperatures exceeding 900 °C, leading to the creation of extra porosity within the CMOF-5 structure. To gain a greater understanding of the electrical performance of CMOF-5 samples, thin film conductivity measurements are performed and correlated with the Zn/ZnO content (Fig. S9†). To evaluate the electrochemical performance of CMOF-5_*X* samples, cyclic voltammetry (CV), galvanostatic charge–discharge (GCD) analysis, and electrochemical impedance spectroscopy (EIS) are conducted in a two-electrode system (CR2032). While CMOF-5_*X* and Zn foil serve as the cathode and anode, respectively, 3 M zinc trifluoromethanesulfonate ($Zn(CF_3SO_3)_2$) is employed as the aqueous electrolyte. Fig. 3a and S10† show the CV curves and Fig. 3b and S11† the GCD profiles of CMOF-5_*X* samples in the voltage range from 0 to 1.8 V at different scan rates and current densities, respectively. The CV and GCD profiles suggest a hybrid nature of the CMOF-5 electrodes. The quasi-rectangular shape of the CV curves and the nonlinear behavior of the GCD profiles imply a combination of electric double-layer capacitance and faradaic charge storage mechanisms, characteristic of asymmetric/hybrid energy storage systems.[30] Among the samples, MOF-5 carbonized at 1000 °C exhibits the largest curve area and the most rectangular CV shape at a scan rate of 1 mV s^{-1} as well as the longest discharge time in the GCD profile at 0.1 A g^{-1}, indicating superior electrochemical performance. Despite varying scan rates and current densities (Fig. S10 and S11†), both CV and GCD profiles exhibit minimal deformation at high rates, indicating rapid kinetics and efficient energy storage behavior. In hybrid/asymmetric devices, we encounter nonlinear GCD profiles (Fig. 3b and S11†), so it is necessary to determine the value of specific capacitance from CV curves (Fig. 3c and Table S3†).[31] The lowest carbonization temperature (600 °C) exhibits a maximum specific capacitance of 133.51 F g^{-1} at 1 mV s^{-1}. Although electrical conductivity slightly improves at 700 °C, the formation of ZnO species disrupts the structural integrity and blocks the porous network. As a result, the capacitance of

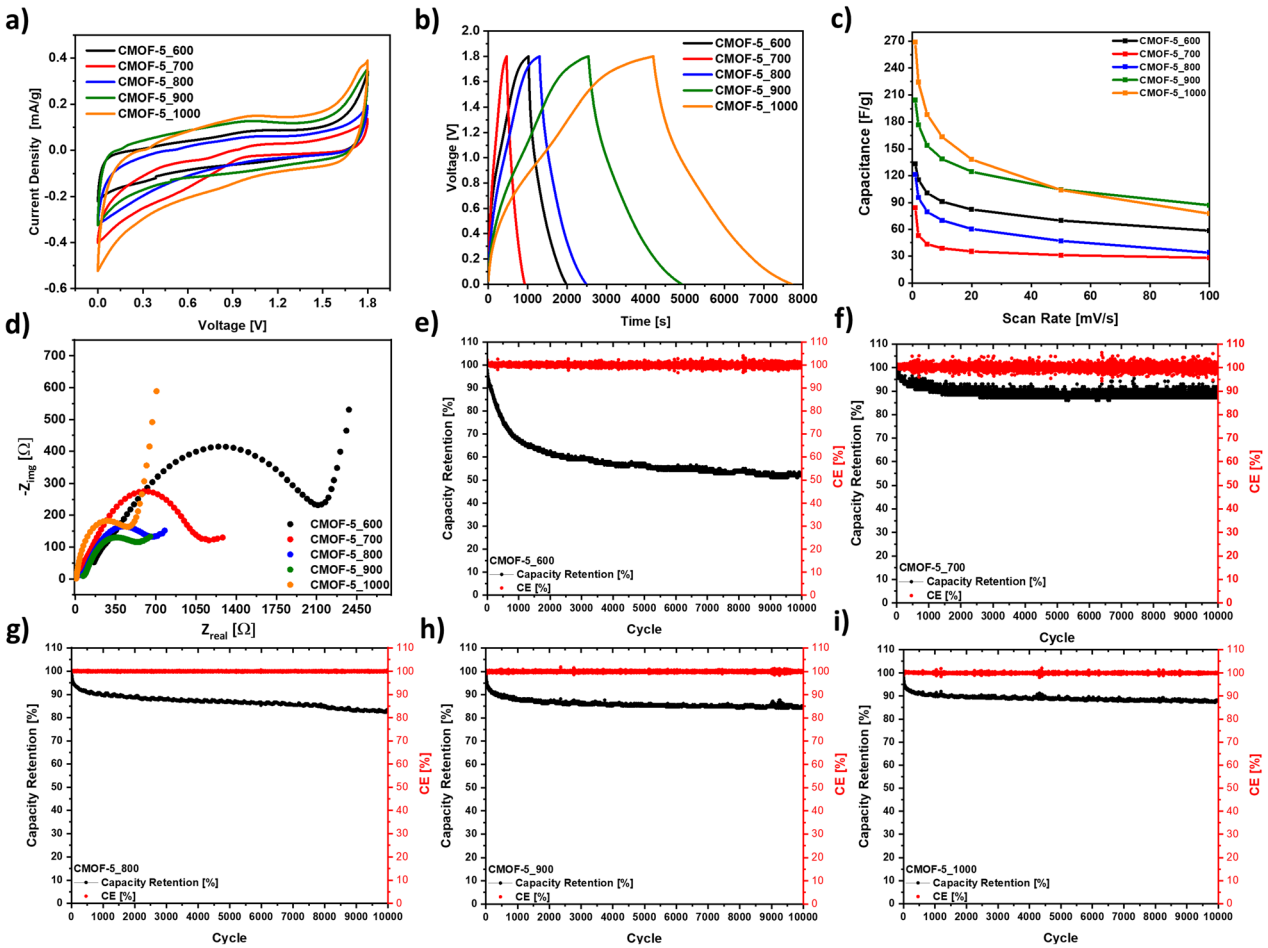

Fig. 3 (a) CV curves at a scan rate of 1 mV s^{-1}, (b) GCD profiles at a current density of 0.1 A g^{-1}, (c) capacitance values at various scan rates, and (d) Nyquist plots for all CMOF-5 samples, cycling stability test after 10 000 cycles for (e) CMOF-5_600, (f) CMOF-5_700, (g) CMOF-5_800, (h) CMOF-5_900, and (i) CMOF-5_1000.

CMOF-5_700 drops to 84.11 F g^{-1}. Starting at 800 °C, as supported by XPS, BET and electrical conductivity analyses, carboreduction takes place, driving the migration of zinc species to the surface. This process not only creates new channels, but also leads to the gradual evaporation of zinc at higher temperatures. As a result, the CMOF-5_800 and 900 samples exhibit specific capacitances of 121.23 and 204.4 F g^{-1}, respectively. Notably, although the CMOF-5_900 sample has lower electrical conductivity compared to CMOF-5_800, its significantly higher porosity enhances ion accessibility and dominates the charge storage process, leading to superior capacitance. The highest capacitance, 268.93 F g^{-1} is achieved for the CMOF-5_1000 sample, representing a 1.43-fold improvement over commercial activated carbon (AC) (Fig. S12†). EIS provides valuable insights into the charge transport behavior of the CMOF-5 samples as a function of carbonization temperature. Nyquist plots (Fig. 3d) are well fitted with the indicated circuit (Fig. S11†). In the chosen equivalent circuit, the internal resistance (R_S) and the charge transfer resistance (R_{CT}) can be determined by the intercept on the real axis and the diameter of the semicircle, respectively (Table S4†).As shown in Fig. 3d, the Nyquist plots exhibit a clear evolution in shape—from a battery-type response for CMOF-5_600 and CMOF-5_700 samples, to a mixed capacitive-battery character for CMOF-5_800 and CMOF-5_900, and finally to a nearly ideal capacitive profile for CMOF-5_1000. Moreover, a significant decrease in the R_{CT} is observed, dropping from 2437 Ω for CMOF-5_600 to just 488.4 Ω for CMOF-5_1000. This substantial reduction in R_{CT} indicates that higher carbonization temperatures enhance the conductivity and optimize the pore structure, allowing more efficient electron and ion transport at the electrode–electrolyte interface.

The cycle stability of CMOF-5_*X* is evaluated at a current density of 1 A g^{-1} (Fig. 3e–i). While carbonization at 600 °C results in only 52% capacitance retention after 10 000 charge/discharge cycles, all samples carbonized at temperatures above 700 °C retain over 85% of their initial capacitance, highlighting the enhanced chemical stability of the materials. This poor stability at 600 °C is likely due to the significant presence of residual ZnO within the carbon matrix, as confirmed by XPS and XRD, which can induce structural degradation during cycling and hinder ion accessibility. In contrast, at higher temperatures (≥900 °C), the effective removal of Zn species and the development of a more stable and conductive porous carbon network contribute to the markedly improved cycling performance. When assessing the potential practical applications of energy storage materials, it is crucial to report power density and energy density. As shown in the Ragone plot (Fig. S14†) the CMOF-5_1000 sample exhibits an impressive maximum energy density of 166.9 W h kg^{-1} and a power density of 9234 W kg^{-1}. Additionally, the kinetics of the electrochemical processes occurring at CMOF-5_*X* electrodes (Fig. S15†) further confirm the truly hybrid nature of the active materials. As the carbonization temperature increases from 700 to 1000 °C, a consistent rise in the diffusion-based contribution can be observed across all the scan rates. This enhancement is attributed to the carboreduction process, which facilitates the removal of surface Zn species, thereby improving the access to internal surfaces and pore channels, as well as enhancing ion diffusion during the charge/discharge cycles. An exception is observed for the CMOF-5_700 sample, where a reduction in diffusion contribution is likely due to the formation of zinc species that disrupt the framework and block pores, limiting ionic transport, in agreement with the reduced capacitance value. Overall, the diffusion-controlled contribution increases from 55% for CMOF-5_600 to 70.9% for CMOF-5_1000 at a scan rate of 1 mV s^{-1}, highlighting the positive impact of high-temperature carbonization on charge storage dynamics.

Compared to previously reported cathode materials for Zn-ion ESS, CMOF-5_1000 delivers a compelling electrochemical performance, with a specific capacitance of 268.93 F g^{-1}, an energy density of 27.8 W h kg^{-1}, and an outstanding power density of 1552.8 W kg^{-1}. While some MOF-derived and carbon-based materials report higher energy densities (*e.g.*, VO0.9/C: 215 W h kg^{-1}),[32] their maximum power densities are significantly lower – typically below 3000 W kg^{-1} (ref. 32) – limiting their rate capabilities. In contrast, CMOF-5_1000 achieves a remarkable balance of high energy and power density, which arises from the synergistic combination of material properties optimized through high-temperature carbonization. The high energy density is largely attributed to a dominant diffusion-controlled contribution (~70.9%), reflecting faradaic charge storage processes supported by a highly porous structure (1.87 cm^3 g^{-1}) and large surface area (2151 m^2 g^{-1}). Meanwhile, the excellent power performance stems from the low charge transfer resistance (488.4 Ω) and improved electrical conductivity (50.15 S m^{-1}) provided by the graphitized carbon matrix, enabling rapid ion and electron transport. Together with excellent cycling stability (88% retention after 10 000 cycles at 1 A g^{-1}), this positions CMOF-5_1000 among the few MOF-derived materials capable of delivering both high energy output and fast charge/discharge performance, making it a strong candidate for high-performance hybrid Zn-ion energy storage devices.

Conclusions

This study demonstrates the critical role of carbonization temperature in tuning the physicochemical and electrochemical properties of MOF-5-derived hybrid materials (CMOF-5_*X*) for Zn-ion energy storage systems. By increasing the carbonization temperature from 600 °C to 1000 °C, we achieve substantial improvements in porosity, and electrical characteristics. The CMOF-5_1000 sample exhibits exceptional characteristics, including a high specific surface area (2151 m^2 g^{-1}), fully developed porosity (1.87 cm^3 g^{-1}), excellent electrical conductivity (50.15 S m^{-1}) and low charge transfer resistance (488.4 Ω). These properties enable a unique combination of high energy density (166.9 W h kg^{-1}) and high power density (9234 W kg^{-1}), along with a specific capacitance of 268.93 F g^{-1} at 1 mV s^{-1}—outperforming commercial activated carbon and many previously reported MOF-derived and carbon materials. The dominant diffusion-controlled contribution (~70.9%) further supports the enhanced energy storage capability, while 88% capacitance retention after 10 000 cycles at 1 A g^{-1}

confirms long-term stability. These results highlight the effectiveness of temperature-tuned carbonization as a scalable strategy for engineering MOF-based electrodes that deliver both high energy output and rapid charge/discharge performance in hybrid Zn-ion energy storage devices.

Data availability

Data for this article, including raw data for Raman, BET, XRD, TGA, SEM, XPS, probe station measurements as well as electrochemical data (GCDs, EIS and CV) are available at Seafile Unistra Repository at **https://shorturl.at/01MgT**. Once the article will be accepted for print all the data will be made available (full open access) at the french national open access database HAL (**https://hal.science**).

Conflicts of interest

There are no conflicts to declare.

Acknowledgements

This work was supported by the National Science Centre (grant no. 2022/47/D/ST5/00261 and 2023/51/B/ST11/00504), the IDUB-AMU program "50 × 50: fifty grants for 50 young scientists – 140/04/POB3/0009, the Interdisciplinary Thematic Institute SysChem *via* the IdEx Unistra (ANR-10-IDEX-0002) within the program Investissement d'Avenir program, the International Center for Frontier Research in Chemistry (icFRC) and the Institut Universitaire de France (IUF).

References

1 D. Larcher and J.-M. Tarascon, *Nat. Chem.*, 2015, **7**, 19–29.
2 P. Poizot, F. Dolhem and J. Gaubicher, *Curr. Opin. Electrochem.*, 2018, **9**, 70–80.
3 X. Mu, H. Pan, P. He and H. Zhou, *Adv. Mater.*, 2020, **32**, 1903790.
4 D. Kundu, B. D. Adams, V. Duffort, S. H. Vajargah and L. F. Nazar, *Nat. Energy*, 2016, **1**, 16119.
5 F. Wang, O. Borodin, T. Gao, X. Fan, W. Sun, F. Han, A. Faraone, J. A. Dura, K. Xu and C. Wang, *Nat. Mater.*, 2018, **17**, 543–549.
6 T. Mageto, S. D. Bhoyate, K. Mensah-Darkwa, A. Kumar and R. K. Gupta, *J. Energy Storage*, 2023, **70**, 108081.
7 H. Peng, Y. Zheng, C. Antheaume, P. Samorì and A. Ciesielski, *Chem. Commun.*, 2022, **58**, 6689–6692.
8 H. Peng, S. Huang, V. Montes-García, D. Pakulski, H. Guo, F. Richard, X. Zhuang, P. Samorì and A. Ciesielski, *Angew. Chem., Int. Ed.*, 2023, **62**, e202216136.
9 H. Peng, V. Montes-García, J. Raya, H. Wang, H. Guo, F. Richard, P. Samorì and A. Ciesielski, *J. Mater. Chem. A*, 2023, **11**, 2718–2725.
10 S. Jia, L. Li, Y. Shi, C. Wang, M. Cao, Y. Ji and D. Zhang, *Nanoscale*, 2024, **16**, 1539–1576.
11 Y. Wang, H. Chen, S. Zhang, L. Hou, X. Li and C. Yuan, *Energy*, 2024, **4**, 100119.
12 J. Liu, Z. Shen and C.-Z. Lu, *J. Mater. Chem. A*, 2024, **12**, 2647–2672.
13 D. Sui, M. Wu, K. Shi, C. Li, J. Lang, Y. Yang, X. Zhang, X. Yan and Y. Chen, *Carbon*, 2021, **185**, 126–151.
14 X. Chen, J.-H. Liu, H. Jiang, C. Zhan, Y. Gao, J. Li, H. Zhang, X. Cao, S. Dou and Y. Xiao, *Energy Storage Mater.*, 2024, **65**, 103168.
15 A. Berman and M. Epstein, *J. Phys. IV*, 1999, **9**, Pr3.
16 I. Vishnevetsky, M. Epstein and R. Rubin, in *Solar Energy*, ASMEDC, Portland, Oregon, USA, 2004, pp. 533–545.
17 K. Cendrowski, P. Skumial, P. Spera and E. Mijowska, *Mater. Des.*, 2016, **110**, 740–748.
18 S. Shin, H. Yoon, Y. Yoon, S. Park and M. W. Shin, *Microporous Mesoporous Mater.*, 2021, **311**, 110726.
19 Y. Wang and Q. Zhang, *RSC Adv.*, 2023, **13**, 18145–18155.
20 S. J. Yang, T. Kim, J. H. Im, Y. S. Kim, K. Lee, H. Jung and C. R. Park, *Chem. Mater.*, 2012, **24**, 464–470.
21 Y.-X. Wang, J. Sun, X. Fan and X. Yu, *Ceram. Int.*, 2011, **37**, 3431–3436.
22 S. Talam, S. R. Karumuri and N. Gunnam, *ISRN Nanotechnol.*, 2012, **2012**, 1–6.
23 F. Ghahramanifard, A. Rouhollahi and O. Fazlolahzadeh, *Superlattices Microstruct.*, 2018, **114**, 1–14.
24 C. Valentini, V. Montes-García, P. A. Livio, T. Chudziak, J. Raya, A. Ciesielski and P. Samorì, *Nanoscale*, 2023, **15**, 5743–5755.
25 J. Chen, T. Shi, T. Cai, T. Xu, L. Sun, X. Wu and D. Yu, *Appl. Phys. Lett.*, 2013, **102**, 103107.
26 A. Apriwandi, E. Taer, R. Farma, R. N. Setiadi and E. Amiruddin, *J. Energy Storage*, 2021, **40**, 102823.
27 M. Härmas, T. Thomberg, H. Kurig, T. Romann, A. Jänes and E. Lust, *J. Power Sources*, 2016, **326**, 624–634.
28 F. J. Martín-Jimeno, F. Suárez-García, J. I. Paredes, M. Enterría, M. F. R. Pereira, J. I. Martins, J. L. Figueiredo, A. Martínez-Alonso and J. M. D. Tascón, *ACS Appl. Mater. Interfaces*, 2017, **9**, 44740–44755.
29 V. V. Kutarov, Y. I. Tarasevich, E. V. Aksenenko and Z. G. Ivanova, *Russ. J. Phys. Chem. A*, 2011, **85**, 1222–1227.
30 S. Sharma and P. Chand, *Results Chem.*, 2023, **5**, 100885.
31 Y. Shao, M. F. El-Kady, J. Sun, Y. Li, Q. Zhang, M. Zhu, H. Wang, B. Dunn and R. B. Kaner, *Chem. Rev.*, 2018, **118**, 9233–9280.
32 Y. Liu, A. Umar and X. Wu, *Rare Met.*, 2022, **41**, 2985–2991.

